

A Graph Attention-Guided Diffusion Model for Liver Vessel Segmentation

Xiaotong Zhang, Alexander Broersen, Gonnice CM van Erp, Silvia L. Pinteá, and Jouke Dijkstra*

Abstract—Improving connectivity and completeness are the most challenging aspects of small liver vessel segmentation. It is difficult for existing methods to obtain segmented liver vessel trees simultaneously with continuous geometry and detail in small vessels. We proposed a diffusion model-based method with a multi-scale graph attention guidance to break through the bottleneck to segment the liver vessels. Experiments show that the proposed method outperforms the other state-of-the-art methods used in this study on two public datasets of 3D-ircadb-01 and LiVS. *Dice* coefficient and *Sensitivity* are improved by at least 11.67% and 24.21% on 3D-ircadb-01 dataset, and are improved by at least 3.21% and 9.11% on LiVS dataset. *Connectivity* is also quantitatively evaluated in this study and our method performs best. The proposed method is reliable for small liver vessel segmentation.

Index Terms—Segmentation, Liver vessel, Computed tomography, Diffusion model, Graph attention.

I. INTRODUCTION

LIVER cancer is the fourth leading cause of death according to the statistics on cancer-related mortality [21]. Furthermore, the liver is a frequent site for metastasis from various primary tumors, such as gastrointestinal tumors, breast cancer, lung cancer and melanoma [8]. Both primary and secondary liver cancer have multiple treatment options including surgery and various interventional oncology liver treatments. The preoperative planning of those treatments can be improved with accurate liver vessel segmentation [1], [25]. In the preoperative planning of liver tumor resection [1], visualizing the spatial location between liver vessels and tumors in a 3D view is one of the essential steps to reduce the surgical risk. Liver vessel segmentation is mainly used to ensure that no main vessels are located near the planned resection region to reduce bleeding. Besides that, liver vessel segmentation is also an important indicator for the Couinaud classification [1], that divides the liver into eight functionally independent regions based on the blood flow of the vascular systems. Hence, accurate liver vessel segmentation plays an important role in liver tumor surgery. Furthermore, it can assist in targeting the correct tumor nutrient supply vessel to decrease the recurrence rate in embolic therapies [14]. However, acquiring accurate and continuous segments of liver vessels is very challenging

This work was supported by China Scholarship Council under Grant 202108310010. (Corresponding author: Jouke Dijkstra.)

Xiaotong Zhang, Alexander Broersen, Gonnice CM van Erp, Silvia L. Pinteá, and Jouke Dijkstra are with the Radiology department, Leiden University Medical Center, Leiden 2333 ZA, The Netherlands (e-mail: {x.zhang, a.broersen, g.c.m.van_erp, s.l.pinteá, j.dijkstra}@lumc.nl).

*This work has been submitted to the IEEE for possible publication. Copyright may be transferred without notice, after which this version may no longer be accessible.

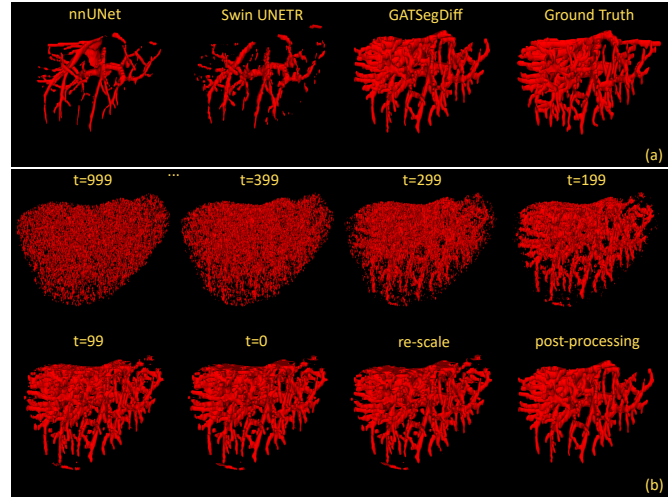


Fig. 1. (a) Comparison between ground truth and different deep network models: our proposal (*GATSegDiff*), *nnUNet* [17] and *Swin UNETR* [12]. It is challenging to ensure vessel continuity in all directions, and to localize small vessels. (b) Liver vessel segmentations generated by our method at different prediction iterations (with 0 being the final iteration).

due to their complex anatomy such as small vessels, especially in low-contrast situations.

Automatic liver vessel segmentation is traditionally done by vessel enhancement relying on image filtering [19], [35], using active contour models [6], [7], or employing tracking methods [4], [9]. These approaches require manual hyper-parameter tuning, initialization of seed-points, or added domain-knowledge. Currently, deep artificial networks and specifically convolutional neural networks (CNN) provide an end-to-end learning paradigm for medical image segmentation and achieve remarkable results [15], [18]. CNNs such as *nnUNet* [17] can extract features automatically from the images with limited manual input. However, locating vessels and ensuring vessel continuity is challenging for CNN-based methods, as shown in Fig. 1(a). To improve the continuity of the segmented vessel tree, self-attention [42] and graph-attention methods [20], [46] are used. However, Fig. 1(a) shows that the attention-based *Swin UNETR* [12] cannot deal with horizontally distributed vessel trees. Overall, it remains challenging to ensure vessel continuity in all directions, and to localize small vessels.

In this paper, we address these two challenges: ensuring vessel continuity and segmenting small vessels. To ensure vessel continuity, we start from a 2D diffusion model [13], [28]. We opt for a 2D rather than a 3D diffusion model to reduce computational requirements. We add graph-attention

layers [3] into the diffusion model to improve the vessel continuity. To compensate for the graph sparsity, we integrate neighboring features of the graph nodes in a local ensemble module of the local implicit image function (LIIF) [5]. The local ensemble module ensures a smooth transition between different nodes [5]. Additionally, to segment small vessels, we extract features at multiple scales in the nodes of the graph. The effectiveness of these components is shown in Fig. 1(b), where we exemplify predictions of our model over different prediction iterations.

This work makes the following contributions: (i) A novel graph attention conditioning diffusion model for vessel segmentation; (ii) An improved continuity and detection of small liver vessels relying on multi-scale graph-features which are used to condition the diffusion model; (iii) A more accurate and continuous vessel segmentation on two public datasets *3D-ircadb-01* [34] and *LiVS* [10], when compared to existing work.

II. RELATED WORK

Liver vessel segmentation. Liver vessel segmentation is currently building on *CNN* methods and attention methods. Based on network structure, *CNN* methods can be divided into methods that rely on *FCN* (fully convolutional networks) [16], [18] and methods that follow the *UNet* architecture [15], [44]. On the other hand, attention methods can be categorized into self-attention-based [38], [42] and graph-attention-based [20], [46] methods. *CNN*-based models such as *UNet* [29] and its variants are the most efficient architecture for medical segmentation, but their performance easily drops when the classes are imbalanced [47]. Moreover, their performance is limited by the receptive-field size of the convolutions [23]. Additionally, for liver vessel segmentation there is a severe data imbalance between the vascular region and the liver region. Although the pixel-level data imbalance of liver vessels segmentation can be mitigated by a variant of the *Dice* loss [15], *CNN* methods are still challenged by long-range dependencies [12]. These limitations lead to incomplete and discontinuous liver vessel segmentations. To address the discontinuous segmentations, *Swin-transformer* [24] uses position encodings to represent the relative input positions, while having a receptive-field size that covers the complete input resolution. Similarly, graph-attention networks [37] rely on an explicit graph to compute node attention-coefficients, which are useful for capturing long-range feature dependencies in the graph. Liver vessel segmentation can take advantage of both the convolution and attention mechanisms, such as augmenting the *UNet* by *Swin-transformer* [42], or using the graph-attention to assist the *UNet* training [20].

Diffusion models for medical image segmentation. Diffusion [13] methods have recently become popular in medical image segmentation, showcasing promising results. These diffusion methods for medical segmentation can be categorized into: non-dynamic conditioning [40] and dynamic conditioning [41], [43]. Non-dynamic conditioning methods are time-independent. The non-dynamic models typically concatenate medical images to the input of the diffusion model, along

the channel dimension. These models cannot provide adaptive conditioning to the diffusion model, based on the model's ability to denoise at each timestep. Their performance [2], [40] is comparable to (or lower than) *nnUNet* [17], which is the standard medical segmentation baseline. On the other hand, dynamic conditioning methods [43] typically use an extra encoder to generate time-dependent conditioning information for the diffusion model. However, these models which are constrained by the diffusion loss only [43], just slightly exceed the segmentation precision of other existing methods. Therefore, more recently *MedSegDiff* [41] proposes a hybrid constrained method which achieves state-of-the-art results. Besides the additional encoder, *MedSegDiff* also has a separate decoder to provide an auxiliary segmentation. Thus, the final result of *MedSegDiff* is a weighted combination of the diffusion segmentation and the auxiliary segmentation. This combination increases the model complexity, and weakens the contribution of the diffusion model.

Graph-based methods for medical image segmentation.

Graphs are one of the most intuitive manners to represent geometric structure, and can be used to model complex anatomical structures. Graphs are defined by a set of nodes and edges connecting the nodes. Graph-based methods for medical image segmentation are known to be used in tree-structure segmentation [30], [31], but are also useful for non-structural medical segmentation [33], [36]. Although, the graph-based methods can be used in combinations with deep networks to prompt the deep network to learn long-range anatomical structures, prior work reports that the fine branches may be missing [22]. This may be due to the sparsity of the nodes causing useful features to be ignored by the node sampling.

Our proposed method for the liver vessel segmentation relies on the capabilities of *CNNs* and attention mechanisms. However, we take this one step further, by aiming to further improve vessel segmentation and jointly enforce continuity by relying on hybrid diffusion mechanisms. In contrast to *MedSegDiff* [41], our proposal fully depends on diffusion predictions for liver vessel segmentation, without using an auxiliary segmentation. We build on the strengths of 2D dynamic conditioning diffusion model, constrained by a hybrid loss. Additionally, we incorporate geometric information about the vessel tree by using graph-attention as a condition. To mitigate the problem of missing fine branches, we use the local ensemble module of LIIF [5], which creates smooth feature transitions between nodes. Additionally, for detecting small vessels we use multiscale features computed over the graph nodes.

III. DIFFUSION CONDITIONING MODELS

Our proposed *GATSegDiff* model is divided into three parts: A. the vanilla conditioning diffusion model using a set of three CT slices for conditioning; B. dynamic conditioning diffusion, starting from the same set of CT slices but using a separate encoder; and C. conditioning diffusion model with multiscale graph-attention guidance. Fig. 2 shows the overall model

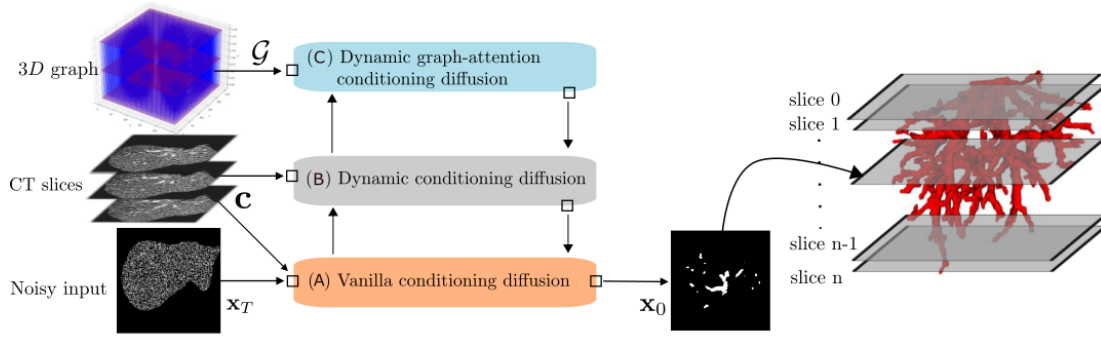


Fig. 2. **Overview of our proposed GATSegDiff model.** GATSegDiff is composed of three components: A. a vanilla diffusion model starting from noisy images \mathbf{x}_T and predicting segmentation masks \mathbf{x}_0 (depicted in orange); B. a dynamic conditioning model, conditioned on three CT slices \mathbf{c} (depicted in gray); and C. a multiscale graph-attention conditioning model, starting from a graph structure \mathcal{G} (depicted in blue). These three components are interconnected, and thus share information.

architecture. Next we provide details about each component, separately.

A. Vanilla conditioning diffusion model

Diffusion model. Conditioning diffusion models are build on top of the Denoising Diffusion Probabilistic Models (DDPM) [13]. DDPM is composed of a forward process and a reverse process.

The forward process gradually adds Gaussian noise to the inputs \mathbf{x}_0 over a number of T timesteps. In our case \mathbf{x}_0 represents the ground truth vessel segmentation mask. The variance of the Gaussian noise is modeled by β_t , which is typically a linear function of t . Thus, the distribution of the noisy vessel mask \mathbf{x}_t given the ground truth \mathbf{x}_0 , is:

$$q(\mathbf{x}_t|\mathbf{x}_0) = \mathcal{N}(\mathbf{x}_t; \sqrt{\bar{\alpha}_t}\mathbf{x}_0, (1 - \bar{\alpha}_t)I), \quad (1)$$

where $\bar{\alpha}_t = \prod_{s=1}^t (1 - \beta_s)$. Therefore, in the forward process, the noisy vessel mask \mathbf{x}_t can be obtained from \mathbf{x}_0 as:

$$\mathbf{x}_t = \sqrt{\bar{\alpha}_t}\mathbf{x}_0 + \sqrt{1 - \bar{\alpha}_t}\epsilon_t, \quad (2)$$

where $\epsilon_t \sim \mathcal{N}(0, I)$.

In the reverse process, the aim is to learn a model p_θ with parameters θ , to iteratively denoise an input noisy image \mathbf{x}_T to recover the clean segmentation mask \mathbf{x}_0 . This also follows a Gaussian distribution:

$$p_\theta(\mathbf{x}_{t-1}|\mathbf{x}_t) = \mathcal{N}(\mathbf{x}_{t-1}; \mu_\theta(\mathbf{x}_t, t), \Sigma_\theta(\mathbf{x}_t, t)). \quad (3)$$

The mean $\mu_\theta(\mathbf{x}_t, t)$ and variance $\Sigma_\theta(\mathbf{x}_t, t)$ of the reverse process can be written as a function of a noise model $\epsilon_\theta(\mathbf{x}_t, t)$. The noise ϵ_θ is typically modelled by a UNet-like architecture [15], [29]. The UNet noise model ϵ_θ is trained by minimizing the difference between the estimated noise ϵ_θ and the true noise ϵ_t at a number of sampled timesteps $t \sim [1, T]$:

$$L_{\text{den}}(\mathbf{x}_0, \theta) = \mathbb{E}_{t \sim [1, T], \mathbf{x}_0, \epsilon_t} \|\epsilon_t - \epsilon_\theta(\mathbf{x}_t, t)\|^2. \quad (4)$$

Conditioning diffusion models. Following [40], we add a conditioning to the DDPM model that is independent of the timestep t . We use three consecutive CT slices, \mathbf{c} , as conditioning for our DDPM model. We evaluate the effectiveness of the vanilla conditioning model in the experimental section.

B. Dynamic conditioning model

Vanilla conditioning cannot provide an adaptive condition for the diffusion process at different noise levels (time steps). To accomplish this, at every diffusion timestep t , we embed the CT slices, \mathbf{c} , by using the *GenericUNet* encoder from *nnUNet* [17], giving rise to \mathbf{f}_c^t . To obtain time-dependent conditioning, we merge the CT-slice embeddings, \mathbf{f}_c^t , at each timestep t into the bottleneck of the *vanilla conditioning diffusion model*, as shown in Fig. 3(ii) (with a solid downward arrow). Additionally, to preserve the contextual information of the CT slices, we use group convolutions and, thus, keep the features per slice separate. We also connect the noisy features of the *vanilla conditioning model* by merging these per layer into the dynamic conditioning model, at appropriate depth (in Fig. 3(ii) with dashed arrows). This has the effect of dynamically changing the CT embeddings at each timestep t .

C. Multiscale graph-attention conditioning model

The vanilla conditioning and the dynamic conditioning both are trained using the denoising loss in Eq. (4). However, we want to make use of the fact that the vessels are continuous across the CT slices. Moreover, the vessels have geometric structure that can easily be mapped into a graph. Thus, we make use of this geometric structure by first mapping the 3D vessel tree into a graph \mathcal{G} . And, subsequently, we rely on graph-attention [3] to integrate this geometric structure as a condition into the diffusion model.

Vessel graph construction. We construct a 3D vessel graph $\mathcal{G}=(\mathbf{V}, \mathbf{E})$, where the nodes \mathbf{V} represent sampled locations along the vessel, and the edges \mathbf{E} indicate the vascular connectivity. During training, we start from the full volume $[D \times H \times W]$ of a ground truth vessel tree, and we split it into non-overlapping sub-volumes $[d \times h \times w]$. Each node $\mathbf{v} \in \mathbf{V}$ in the graph is calculated by averaging the voxel coordinates along the vessel region for that specific sub-volume. If there is no vascular annotation in a sub-volume, we use the central voxel as the node. To define the graph edges, $\mathbf{e} \in \mathbf{E}$, we calculate the geodesic distance between nodes, as in *VGN* [31]. We want to avoid connecting two nodes with a small distance but belonging to different vessel branches. For this

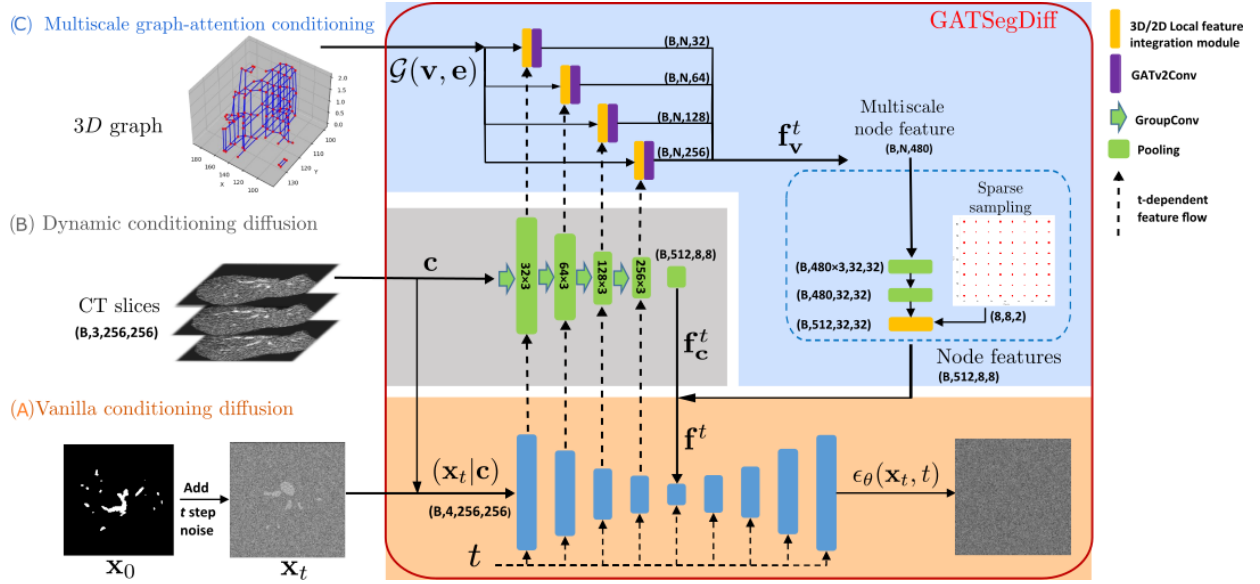


Fig. 3. **Network architecture of GATSegDiff.** Our model is composed of three components: A. the vanilla conditioning diffusion (in orange); B. the dynamic conditioning diffusion (in gray); C. the multiscale graph-attention conditioning (in blue). These components interact with each other, as indicated through the vertical (dashed arrows) going upwards from the vanilla diffusion model, and downwards (in solid arrows) from adding the conditioning features: CT slices — c , CT slice embeddings — f_c^t , and graph embeddings — f_v^t .

we use the binary vessel label as a speed function to calculate the travel time from a node to another node, as in [20].

Graph in training and inference. In the training phase, we construct the graph \mathcal{G} using the ground truth vessel masks. Each input consists of 3 consecutive CT images, as shown in Fig. 3. Note, that only the foreground nodes, corresponding to the true location of the vessels, are displayed in Fig. 3(C), while the background nodes are displayed as transparent. During inference, we do not have access to the ground truth vessel masks, therefore, we input to the multiscale graph-attention conditioning model (C) a fully-connected graph, as shown in Fig. 2. Using a fully-connected graph at inference is a viable choice, because the graph is only useful during training the weights of the component (C) and focusing them via the graph-attention on the informative features received from component (B). At inference, these weights are trained and can be applied on the new input features coming from component (B). In the ablation studies in Section IV-C we demonstrate that effectiveness of using the fully-connected graph at inference.

Multiscale graph-attention. We use the CT-slice embeddings, f_c^t , computed over the *dynamic conditioning model* to extract node features at every node and every timestep t (depicted in Fig. 3(iii) via the dashed upward arrows). We process the node features via a graph-attention layer GATv2 [3] and a local feature integration module (LIIF) [5], to obtain node attention-coefficients. These node attention-coefficients are concatenated over the different scales (network depths), coming from the *dynamic conditioning model*, giving rise to multiscale node attention-coefficients: f_v^t at each node v and timestep t .

Due to the sparsity of the nodes in the vessel graph \mathcal{G} (only 32×32 nodes for one CT slice), we lose information contained in the CT-embeddings f_c^t . To compensate for this information

loss, we adopt the local features integration module LIIF [5] which is widely used for image super-resolution. We extend this module from 2D to 3D, and apply it on our CT-embeddings f_c^t using the graph neighborhood information. Specifically, for a CT-slice embedding $f_c^{(t,i)}$ at timestep t and location i corresponding to a graph node v_i , we use the graph neighboring locations $v_{i'}$ to define a new embedding:

$$\hat{f}_c^{(t,i)} = \sum_{i'} \frac{\mathcal{S}(v_i, v_{i'})}{\mathcal{S}(v_i, v_{i'}) \text{LFI}(f_c^{(t,i')}, (v_i - v_{i'}))}, \quad (5)$$

where in our case the neighboring locations i' vary across x, y , and z directions, rather than just x, y ; and $\mathcal{S}(v_i, v_{i'})$ computes the area of a 2D rectangle, or a 3D cube between the graph node v_i and its neighboring mode $v_{i'}$; and $\text{LFI}(\cdot)$ is the standard local feature integration module from [5].

Subsequently, we use new CT-slice embeddings $\hat{f}_c^{(t,i)}$ to extract node features via a graph-attention layer GATv2 [3], for every two neighboring locations i, j :

$$f_v^{(t,i,j)} = \frac{\exp[\mathbf{a}^\top \text{LeakyReLU}(\mathbf{W}(\hat{f}_c^{(t,i)} + \hat{f}_c^{(t,j)}))]}{\sum_{j'} \exp[\mathbf{a}^\top \text{LeakyReLU}(\mathbf{W}(\hat{f}_c^{(t,i)} + \hat{f}_c^{(t,j')})]} \quad (6)$$

During training, the graph structure is computed using the ground truth vessel-tree structure. At inference time, we do not have this information, but we can make use of features trained to recognize if a certain node feature f_v corresponds to a vessel-tree location or not. Therefore, we additionally process the node features via a convolutional layer and sigmoid activations, to obtain $\hat{f}_v^t = \text{sigmoid}(\text{Conv}(f_v^t))$, and optimize a binary cross-entropy graph-loss on these:

$$L_{\text{graph}}(\mathcal{G}, \theta) = - \sum_{v \in \mathcal{G}} \sum_t \log(\hat{f}_v^t), \quad (7)$$

where θ are model parameters.

TABLE I

DATASET OVERVIEW. *3D-ircadb-01* [34] PROVIDES ANNOTATIONS ON EVERY CT SLICE, BUT MISSES SMALLER VESSEL ANNOTATIONS. *LiVS* [10] CONTAINS MORE CT VOLUMES BUT ONLY A SUBSET OF THE SLICES ARE ANNOTATED.

	<i>3D-ircadb-01</i>	<i>LiVS</i>
Available scans	20	532
Used scans	20	303
Exclusion	'completeness score'; CT thickness $\geq 2.5\text{mm}$	#annotation (< 30 slices); CT thickness $\geq 5\text{mm}$
Pixel spacing	0.57mm – 0.87mm	0.51mm – 0.98mm
Slice thickness	1.0mm – 4.0mm	0.62mm – 5.0mm

Overall diffusion model conditioning

We use the multiscale graph-attention coefficients \mathbf{f}_v^t together with the CT embeddings as conditioning for the reverse diffusion process. Therefore, Eq. (3) defining the reverse process, has to be updated to incorporate the conditioning \mathbf{f}^t at timestep t :

$$p_\theta(\mathbf{x}_{t-1}|\mathbf{x}_t) = \mathcal{N}(\mathbf{x}_{t-1}; \mu_\theta(\mathbf{x}_t|\mathbf{f}^t, t), \Sigma_\theta(\mathbf{x}_t|\mathbf{f}^t, t))$$

$$\mathbf{f}^t = \mathbf{f}_c^t(\mathbf{x}_t, \mathbf{c}) + \mathbf{f}_v^t(\mathbf{x}_t, \mathbf{c}, \mathcal{G}), \quad (8)$$

where $\mathbf{f}_c^t(\cdot)$ are the dynamic CT embeddings, and $\mathbf{f}_v^t(\cdot)$ are the node attention-coefficients over the CT slices, \mathbf{c} .

Overall loss function

The total loss function, used during training to fit the overall model parameters θ , is a combination of the denoising loss in Eq. (4) and graph loss in Eq. (7):

$$L_{\text{total}}(\mathbf{x}_0, \mathbf{c}, \mathcal{G}, \theta) = L_{\text{den}}(\mathbf{x}_0, \mathbf{c}, \mathcal{G}, \theta) + L_{\text{graph}}(\mathcal{G}, \theta), \quad (9)$$

where the denoising loss L_{den} also contains the CT-slice \mathbf{c} embeddings and the graph \mathcal{G} for conditioning.

IV. EXPERIMENTAL ANALYSIS

Datasets overview. We use two public datasets in this study: *3D-ircadb-01* [34] and *LiVS* [10]. *3D-ircadb-01* is a widely used dataset containing 20 cases. *LiVS* is a recently released 2D liver vessel segmentation dataset containing 532 cases. *3D-ircadb-01* has vessel tree annotations at every slices, but some smaller vessels have not been annotated [15], [44]. On the other hand, *LiVS* is a larger dataset, but the annotations are done only on a subset of randomly chosen slices from the CT volumes. Tab. I shows details about these two datasets.

CT scans with thick slices ($\geq 2.5\text{mm}$ for *3D-ircadb-01* and $\geq 5\text{mm}$ for *LiVS*) are the outliers in the slice thickness distribution. Therefore, we excluded these cases from both the training and test sets for *LiVS*. Considering the limited number of data in *3D-ircadb-01*, we only exclude the thick slice cases from the test set of *3D-ircadb-01*. To effectively evaluate the small *3D-ircadb-01* dataset, we asked a clinical expert to score the completeness of the annotated vessels. Based on these scores we aim to construct a reliable test-set. Cases {04, 06, 08, 11, 16, 18, 19} receive 4 points (out of 5), which means that the annotations are relatively complete. However, the thickness of cases 18 and 19 is greater than

2.5 mm, so we also exclude these from the test-set. Therefore, we use the remaining five cases {04, 06, 08, 11, 16} as the test-set. Given the small set size, we perform leave-one-out cross-validation on these five cases, where at every fold we train on 19 cases (the remaining 15 cases are not part of the test-set, plus 4 cases not used in the current fold). We average the results over all folds. We used 3-fold cross-validation and reported the averaged metrics in the experiments for the *LiVS* dataset.

Data pre- and post-processing. For the *3D-ircadb-01* [34] dataset, we first crop the liver region and resize the cropped CT slices to 256×256 px. The liver masks exclude the vena cava and keep only the small liver vessel. We clip the intensity of the CT slices to $[0, 400]$ HU (Hounsfield units). The CT slices are already cropped, resized, and clipped for the *LiVS* [10] dataset. Because not all slices are annotated, we use ITK-SNAP [45] to interpolate the annotations. In our method, we sample the central slice of the 2.5D block only among the CT slices that have provided ground truth annotations.

During inference, we rescale the diffusion results for each slice of the liver vessel tree from the resolution on the image of 256×256 px to the physical resolution on the original CT image of 512×512 px. In the post-processing, we remove additional disconnected noisy spots whose volume is less than 1% of the largest connected region. For this, we perform connected region analysis with SciPy [39].

Evaluation metrics. For all our experiments we report the: Dice similarity coefficient (*DSC*), voxel-wise sensitivity (*Sen*), voxel-wise specificity (*Spe*) [27], centerline Dice (*clDice*) [32] and a customized connected region-wise connectivity (*Con*) following Gegúndez-Arias *et al.* [11]. The *Con* metric is defined as the ratio of the total number of connected regions in the predicted tree \mathcal{T} and the total number of connected regions in the ground truth vessel tree \mathcal{T}^* :

$$\text{Con} = \frac{|\text{comp}(\mathcal{T})|}{|\text{comp}(\mathcal{T}^*)|} \geq 1, \quad (10)$$

where we only consider connected regions with a volume greater than 120 mm^3 , as in Huang *et al.* [15]. A *Con* value less than 1.0 is over-connected or indicates that the segmentation is more accurate than the ground truth. We do not consider these situations here.

Baseline models. We compare our *GATSegDiff* model with four baselines: *MedSegDiff* [41], *EnsemDiff* [40], *Swin UNETR* [12] and *nnUNet* [17]. The *MedSegDiff* [41] and *EnsemDiff* [40] baselines use inputs of size $(3, 256, 256)$, while *Swin UNETR* and *nnUNet* are 3D methods and they receive the cropped CT slices as input, in the default setting. *Swin UNETR* [12], *EnsemDiff* [40] and *MedSegDiff* [41] require an ensemble. For *Swin UNETR*, we train 5 models and ensemble their segmented results. For *EnsemDiff* and *MedSegDiff*, we ensemble 5 diffusion sampling results, but with a single training. Our *GATSegDiff* method does not use ensembles when performing inference with the DDPM sampling [28].

Implementation details. We perform all our experiments on 1 NVIDIA RTX A6000 GPU with 48 GB memory. We use

TABLE II

RESULTS ON THE *3D-ircadb-01* [34] DATASET. WE COMPARE OUR *GATSegDiff* MODEL WITH PRIOR WORK: *MedSegDiff* [41], *EnsemDiff* [40], *Swin UNETR* [12] AND *nnUNet* [17]. OUR METHOD IS THE BEST IN TERMS OF *DSC*, *cIDice*, *Sen* AND *Con* SCORES, BUT WORSE IN *Spe* SCORES. INTERESTINGLY, *nnUNet* HAS THE HIGHEST *Spe* SCORE AND THE LOWEST *Sen* SCORE, WHICH MAY BE DUE TO A TRADE-OFF BETWEEN DETAILED AND ACCURATE SEGMENTATION.

	Representation type	<i>DSC</i> (%)	<i>cIDice</i> (%)	<i>Sen</i> (%)	<i>Spe</i> (%)	<i>Con</i> ($\rightarrow 1$)
<i>nnUNet</i> [17]	3D	58.76 \pm 9.89	71.46 \pm 5.67	43.32 \pm 11.18	100 \pm 0	2.46 (27/11)
<i>Swin UNETR</i> [12]	3D	57.80 \pm 9.93	64.16 \pm 7.10	46.71 \pm 13.21	99.96 \pm 0.02	7.18 (79/11)
<i>EnsemDiff</i> [40]	2.5D	54.82 \pm 9.64	60.61 \pm 9.55	40.05 \pm 10.45	99.98 \pm 0.02	6.27 (69/11)
<i>MedSegDiff</i> [41]	2.5D	59.59 \pm 7.73	66.03 \pm 8.05	47.38 \pm 10.44	99.95 \pm 0.05	8.82 (97/11)
<i>GATSegDiff</i> (ours)	2.5D	71.26 \pm 1.93	74.61 \pm 1.21	71.59 \pm 4.07	99.89 \pm 0.04	1.09 (12/11)

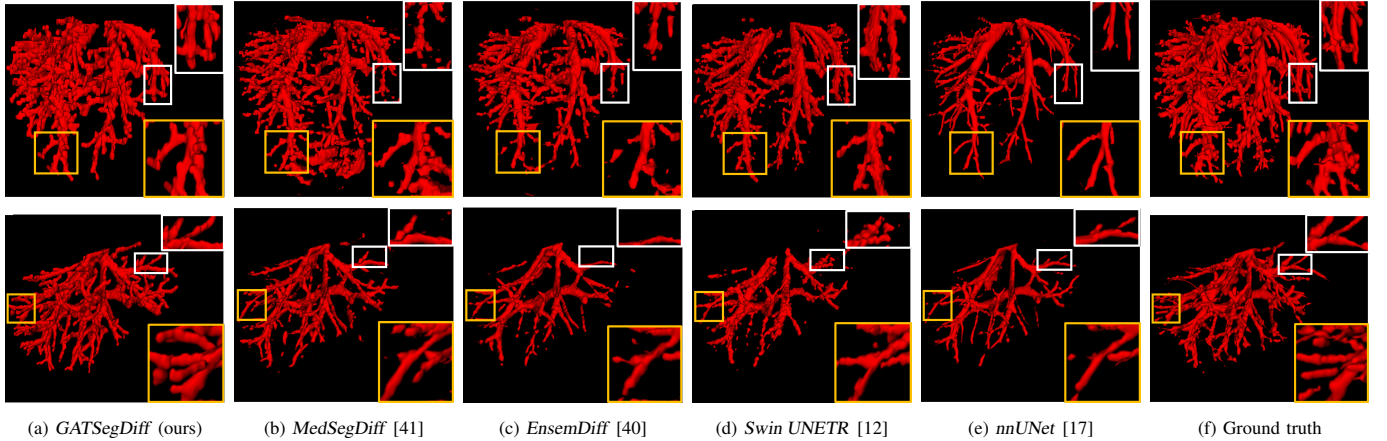


Fig. 4. **Visualizations on the *3D-ircadb-01* [34] dataset.** (a) The liver vessel tree segmented by our proposed *GATSegDiff*; (b), (c), (d) and (e) are the liver vessel tree segmented by the baselines: *MedSegDiff* [41], *EnsemDiff* [40], *Swin UNETR* [12] and *nnUNet* [17], respectively; (f) The ground truth liver vessel tree. The yellow and white boxes compare the completeness and continuity between our proposed model and the baselines. We also show the boxes enlarged in the top/bottom right corners. Our method (1st column) achieves the most similar appearance to the ground truth (6th column) in both fine vessel segmentation and connectivity.

the *AdamW* optimizer with an initial learning rate of 1×10^{-4} and a batch size of 10. We input 4 channels: namely the three CT-slices and a noisy ground truth at a stochastic time step t during training, while we use a random Gaussian noise channel during inference. Our *GATSegDiff* model can converge well within 160k iterations. We train the *EnsemDiff* [40] and *MedSegDiff* [41] models following their official implementation for 60k [40] and 100k [41], respectively. On the *3D-ircadb-01* dataset, we use the standard DDPM sampling scheme [28] with 1000 denoising steps, during inference, for all the diffusion-based experiments. Given that the *LiVS* dataset contains hundreds of cases, the inference with the DDPM is too time-consuming, so we adopt the *DPM-Solver++* [26] with 30 denoising steps, for all the diffusion-based experiments. For our *GATSegDiff* model, the CT block size is (3, 256, 256) and the vessel graph \mathcal{G} consists of nodes of size $(N, 3)$ and edges of size $(E, 2)$. Where we set the number of graph nodes N to 32×32 per CT slice.

A. Comparative experiments on *3D-ircadb-01* dataset

Quantitative evaluation on *3D-ircadb-01*. Tab. II provides the numerical evaluation and compares our proposed *GATSegDiff* model with *MedSegDiff* [41], *EnsemDiff* [40], *Swin UNETR* [12] and *nnUNet* [17]. We group the methods per type of learned network representation: 3D (using 3D convolutions) or 2.5D (using 2D convolutions but 2.5D

CT slices). The 3D non-diffusion methods such as *nnUNet* and *Swin UNETR* are outperformed by *MedSegDiff* but are better than *EnsemDiff*. Intuitively, diffusion-based methods with dynamic conditioning like *MedSegDiff* perform better at segmentation than the non-dynamic conditioning methods like *EnsemDiff*. Although, *EnsemDiff* and *MedSegDiff* and our proposed *GATSegDiff* are built on diffusion models, our method still exceeds them in terms of *DSC* and *Sen* scores. Our *GATSegDiff* improves at least 11.67% and 24.21% in *DSC* and *Sen* compared to all other baselines in Tab. II. These improvements are a result of the graph-attention conditioning in our method.

In Tab. II we also report the standard deviation of the metrics. Our method has the lowest standard deviation for *DSC* and *Sen* compared to the other methods. This indicates that our model tends to make more stable predictions.

Spe evaluates the degree of false positive predictions for a segmented liver vessel tree. *Swin UNETR*, *EnsemDiff* and *MedSegDiff* obtain comparable *Spe* scores. However, our *GATSegDiff* obtains a slightly lower score than the others; we believe that our lower *Spe* scores are explained by the missing small-vessel annotations. Interestingly, in Tab. II, *nnUNet* gets the highest averaged *Spe* but with the lowest averaged *Sen*, which is a trade-off between segmentation accuracy and completeness.

Tab. II also reports vessel connectivity with *cIDice* [32]

and *Con*. *Con* is defined in Eq. (10) which should ideally be as close as possible to 1. Additionally, we also report in the brackets the number of connected regions of the segmented vessel tree and the ground truth. Our method achieves the highest *cIDice* score compared to the baselines, demonstrating that our method can better fit the centerlines of the segmented liver vessel tree to that of the ground truth. *nnUNet* achieves the second highest *cIDice* score, but it is less representative for evaluating the voxel-wise liver vessel segmentation due to the vessel diameter insensitivity of *cIDice*. Although *nnUNet* has the lowest *Sen* score, which means incomplete segmentations, *cIDice* is rarely affected. The *Con* score of our method is the closest value to 1 compared to the other methods, which is indicative of the continuous predictions in our model. Interestingly, *MedSegDiff* is also based on a diffusion model, obtains the worse connectivity score. This may be due to the poor quality of the auxiliary segmentation of *MedSegDiff*.

Qualitative evaluation on 3D-ircadb-01. In Fig. 4 we provide a qualitative evaluation on two test cases from the 3D-ircadb-01 dataset. Compared to the other methods, the appearance of our predicted vessel-tree segmentation (first column) is the most similar to the ground truth (last column). The vascular structure marked by the top-yellow box in the first row, and the left-yellow box in the second row are almost completely segmented by our method, while the other methods miss parts of the vessel tree. Especially the segmentation results of *Swin UNETR* [12] and *nnUNet* [17], are visibly sparse. These results relate to the low *DSC* and *Sen* scores of *Swin UNETR* and *nnUNet* in Tab. II. Although the vessel structures of *EnsemDiff* [40] (third column) and *MedSegDiff* [41] (second column) are denser than those of the non-diffusion methods, they provide more discontinuous vessel masks at the extremities of the tree (*i.e.* for smaller vessels).

The connectivity of the distal liver vessels is shown in Fig. 4. The distal vessel branches marked by the lower-yellow box in the first row and the right-yellow box in the second row show that our segmentation is as continuous as the ground truth. This corresponds to a *Con* score closer to 1 in Tab. II. Comparing the vessel branches of *nnUNet* with the other methods for the distal vessels, we see that these are precise, being exceeded only by our method. This is again consistent with the *Con* score of *nnUNet* in Tab. II – the second best score.

B. Comparative experiments on LiVS dataset

Quantitative evaluation on LiVS. Tab. III compares our *GATSegDiff* with *MedSegDiff* [41] and *EnsemDiff* [40]. The ground truth of the liver vessels is discontinuous in the longitudinal direction, as shown in Fig. 5(d). Thus, the two 3D baselines used on 3D-ircadb-01 dataset are not applicable for LiVS dataset. Similarly, on LiVS we cannot report *Con* scores. In Tab. III, our *GATSegDiff* has the best *DSC* and *Sen* scores. Especially in terms of *Sen*, our *GATSegDiff* performs better than the baselines, indicating a more complete vessel segmentation. Our *GATSegDiff* improves at least 3.21% and 9.11% in *DSC* and *Sen* compared to all other baselines in Tab. III. As with the 3D-ircadb-01 dataset, these improvements

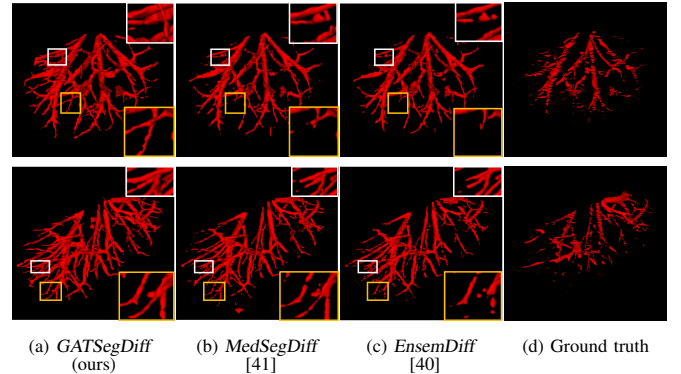


Fig. 5. **Visualizations of the LiVS [10] dataset.** (a) The liver vessel tree segmented by our proposed *GATSegDiff*; (b) and (c) are the liver vessel tree segmented by the baselines: *MedSegDiff* [41] and *EnsemDiff* [40]; (d) The discontinuous (partially annotated) ground truth liver vessel tree. Yellow and white boxes show the completeness and continuity between our proposed model and baselines. These boxes are enlarged in the top/bottom right corner. Our model (1st column) has the most detailed vessel segmentation.

TABLE III
RESULTS ON THE LiVS [10] DATASET. THE PERFORMANCE OF OUR *GATSegDiff* COMPARED WITH *EnsemDiff* [40] AND *MedSegDiff* [41] WITH THE DICE COEFFICIENTS, SENSITIVITY AND SPECIFICITY RESULTS. OUR METHOD OUTPERFORMS THE OTHERS IN TERMS OF *DSC* AND *Sen* SCORES. *Spe* OF OUR MODEL IS SLIGHTLY LOWER THAN *MedSegDiff*, WHICH IS A TRADE-OFF BETWEEN COMPLETENESS (*Sen*) AND ACCURACY (*Spe*) OF VESSEL SEGMENTATION. CONNECTIVITY EVALUATION METRICS *cIDice* AND *Con* ARE NOT APPLICABLE FOR THE LiVS DATASET WITH ITS DISCONTINUOUS GROUND TRUTH.

	Repr. type	DSC (%)	Sen (%)	Spe (%)
<i>EnsemDiff</i> [40]	2.5D	56.68±12.59	56.48±8.41	99.65±0.23
<i>MedSegDiff</i> [41]	2.5D	75.83±5.76	64.33±7.69	99.96±0.03
<i>GATSegDiff</i> (ours)	2.5D	79.04±5.99	73.44±6.99	99.90±0.07

are due to the graph-attention conditioning in our model. Although *MedSegDiff* has lower scores than our *GATSegDiff* for *DSC* and *Sen*, it outperforms the *EnsemDiff* baseline by far. This may be due to the the dynamic conditioning method used in *MedSegDiff*. The standard deviations of our *GATSegDiff* and *MedSegDiff* are comparable, and they are both lower than the standard deviation of *EnsemDiff*. This could indicate that the dynamic conditioning diffusion model (ours and *MedSegDiff*) can provide more stable results than the vanilla conditioning model (*EnsemDiff*).

Qualitative evaluation on LiVS. In Fig. 5, we provide a qualitative comparison in 3D on two test cases between our *GATSegDiff* and the baselines: *MedSegDiff* [41] and *EnsemDiff* [40]. Although it is hard to directly compare the segmentations of the different methods, due to the discontinuous ground truth (shown in Fig. 5(d)), inter-method comparison can still be informative. The yellow boxes in Fig. 5 show that neither *MedSegDiff* nor *EnsemDiff* can segment distal fine vessels, while our segmented vessel structures are denser and more complete.

Fig. 6 shows a qualitative comparison for the slices of two cases, in a 2D cross-sectional view to compare the vessel completeness. Fig. 6(a) to (c) show the overlaid segmentation masks of the liver vessel mask of different methods, when

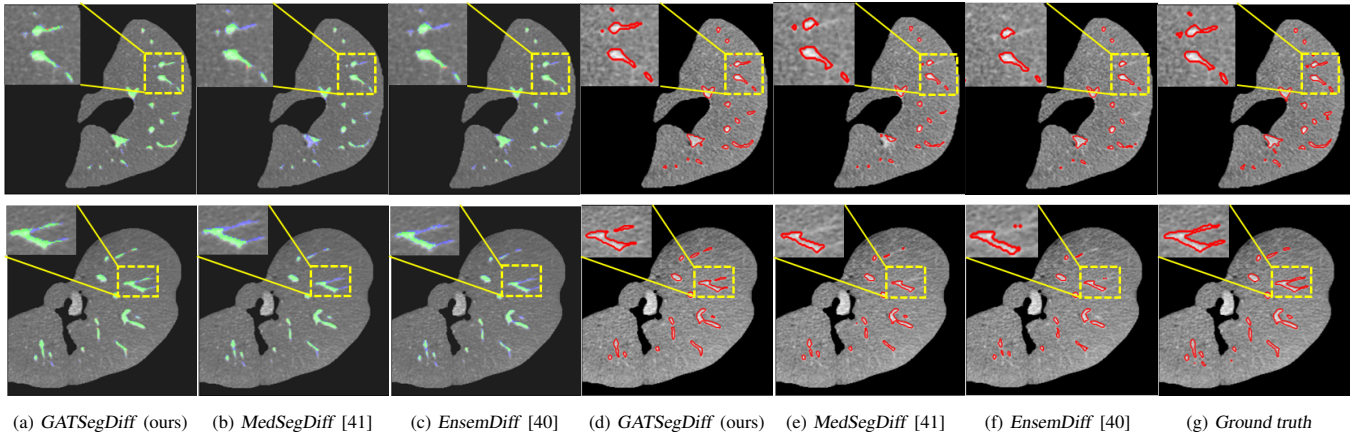


Fig. 6. **Cross-sectional visualizations on LiVS [10] dataset.** We compare segmentation masks from our *GATSegDiff* with *MedSegDiff* [41] and *EnsemDiff* [40]. (a), (b) and (c) show overlaid predicted segmentation masks on top of a CT slice (where green: true positive, red: false positive, blue: false negative); (d) to (g) are the 2D contours obtained from the predictions of different methods, when compared to the ground truth. We highlight in the yellow box differences in predictions. Our method can segment both long-tail and fine vessel structures, while baselines fail in these situations.

TABLE IV

ABLATION STUDY ON 3D-ircadb-01 DATASET. WE ABULATE THE EFFECT OF EACH INDIVIDUAL COMPONENT PRESENTED IN FIG. 3: (I) VANILLA CONDITIONING MODEL; (II) DYNAMIC CONDITIONING MODEL; AND (III) MULTISCALE GRAPH-ATTENTION CONDITIONING. INTERESTINGLY, THE VANILLA MODEL AND THE VANILLA MODEL COMBINED WITH DYNAMIC CONDITIONING PERFORM BEST IN TERMS OF *Spe* SCORES. THIS IS BECAUSE PREDICTING LESS STRUCTURES (LOW *Sen* SCORES) ENTAILS FEWER FALSE POSITIVES. HOWEVER, THE OVERALL COMBINATION PERFORMS BEST ON ALL OTHER METRICS.

(i) Vanilla conditioning [40]	(ii) Dynamic conditioning	(iii) Dynamic multiscale graph-attention conditioning	DCS(%)	clDice(%)	Sen(%)	Spe(%)	Con (\rightarrow 1)
✓	×	×	54.82 \pm 9.64	60.61 \pm 9.55	40.05 \pm 10.45	99.98 \pm 0.02	6.27 (69/11)
✓	✓	×	59.00 \pm 5.43	64.76 \pm 3.74	44.22 \pm 6.19	99.98 \pm 0.01	6.45 (71/11)
✓	✓	✓	71.26 \pm 1.93	74.61 \pm 1.21	71.59 \pm 4.07	99.89 \pm 0.04	1.09 (12/11)

compared to the ground truth mask. Green, red and blue colors represent true positive, false positive and false negative, respectively. The blue areas of the overlaid masks in columns (b) and (c) reflect the missing contours of the baselines. Our *GATSegDiff* has fewer blue regions, indicating that our segmentation is more complete for both the long-tail and small vessel structures. The red contours in Fig. 6(d)-(f) outline the boundary of the predicted liver vessel segmentation of different methods. The contours in the last column (g) correspond to the boundary of ground truth vessel mask. We zoom-in on regions using the yellow boxes, to highlight differences in the vessel completeness. Comparing the contours of *MedSegDiff* and *EnsemDiff* in column (e) and column (f) with the ground truth, long-tail vessel structures and tiny vessel blobs are not outlined. Our *GATSegDiff* model benefits from the long-range feature dependency encoded in the multi-scale graph-attention conditioning.

C. Model ablation study

Effect of different model components. For ease of analysis we perform the ablation studies on the more compact *3D-ircadb-01* dataset. However, we expect our conclusions to be valid across datasets. Because the three components of our model : (i) vanilla conditioning, (ii) dynamic conditioning and (iii) multiscale graph-attention, are highly interconnected (see Fig. 3), we cannot evaluate them independently. To explore the influence of different conditioning levels on the performance

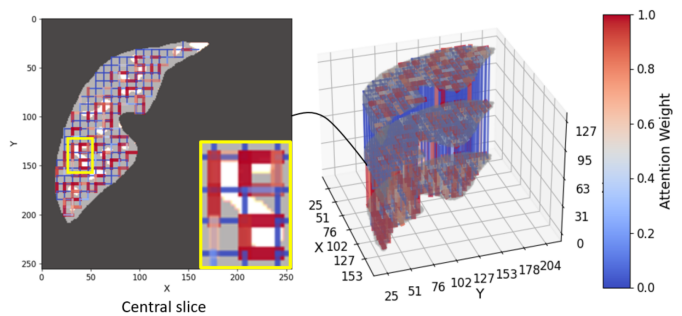


Fig. 7. **Edge attention weights of a fully-connected graph in inference.** Blue/red represent low/high attention weights, respectively. We also show the box enlarged in the bottom right corner. The vessel area and its neighborhood attract more edge attention, thus demonstrating the utility of inputting a fully-connected graph in inference.

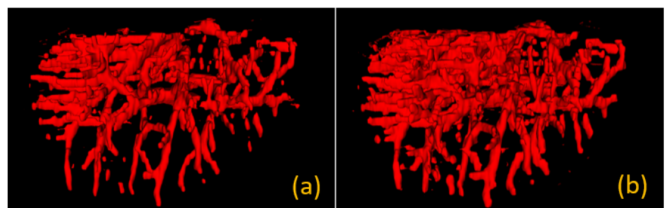


Fig. 8. **Inference difference between using an empty graph, without edges (a) and a fully-connected graph (b) as the input.** Using a fully-connected graph leads to denser more continuous predictions.

of liver vessel segmentation, we perform an additive ablation study in Tab. IV. We start from the (i) vanilla conditioning model and subsequently add new conditioning components to it. Noteworthy, the vanilla model (i) (in the first row) and the combination of the vanilla model with the dynamic conditioning model (ii) (in the second row) achieve the highest *Spe* scores. This is due to these models predicting fewer structures in the segmentation masks (as shown by the low *Sen* score), and therefore having fewer false positives. The final model combining all three components: (i) vanilla conditioning, (ii) dynamic conditioning and (iii) multiscale graph-attention has the highest *DSC*, and *Sen* scores. The *Con* scores of the final combined model are closer to 1 than the other models. The graph-attention conditioning contributes considerably to the performance of our *GATSegDiff* model. Overall, we conclude that all components have a beneficial effect on the vessel segmentation scores.

Graph-attention in inference. In inference, we input a fully-connected graph in the component (C), as shown in Fig. 2. While the node coordinates are uniformly distributed in the graph, the edge weights between nodes are adapted by the trained graph-attention layer. Fig. 7 visualizes the learned edge weights for an input fully-connected graph. In Fig. 7, the cross-sectional view shows that the vessel area and its neighborhood attract more edge attention. Additionally, in Fig. 8 we compare the difference in predictions when inputting an empty graph, without edges (a) and a fully-connected graph (b). A comparison between two inferences, separately using a no-edge graph and a fully-connected graph, is shown in Fig. 8. Using an empty graph leads to sparser predictions. This analysis demonstrates that graph attention layers are still effective, even with a uniform graph as input.

V. DISCUSSION

A. Analysis of model limitations

To analyze the limitation of our *GATSegDiff*, we look in Fig. 9 at the examples with the worst *DSC* scores, for each of *LiVS* and *3D-ircadb-01* datasets. On these worst cases, our proposed *GATSegDiff* inaccurately predicts vessel segmentations when there is a large tumor surrounded by contrast-rich regions, as shown in Fig. 9(a). This failure is reflected by a larger standard deviation in the *DSC* scores of the *LiVS* dataset in Tab. III. All tumors in *3D-ircadb-01* are characterized as low-intensity regions, and are not surrounded by contrast, so this failure appears only on the *LiVS* dataset. Fig. 9(b) shows a worst performing example on the *3D-ircadb-01* dataset. The low *DSC* score is due to missing annotations [15], [44]. The yellow box highlights a case where vessels were not annotated. Our model correctly predicts this (while still being penalized in the *DSC* scores). While with the yellow arrows we indicate regions where our model over-predicts structure that is not present there. The inconsistency in annotation quality in the *3D-ircadb-01* dataset [34] makes the model training extra challenging. This may lead to the model learning to focus on the wrong information when predicting segmentations.

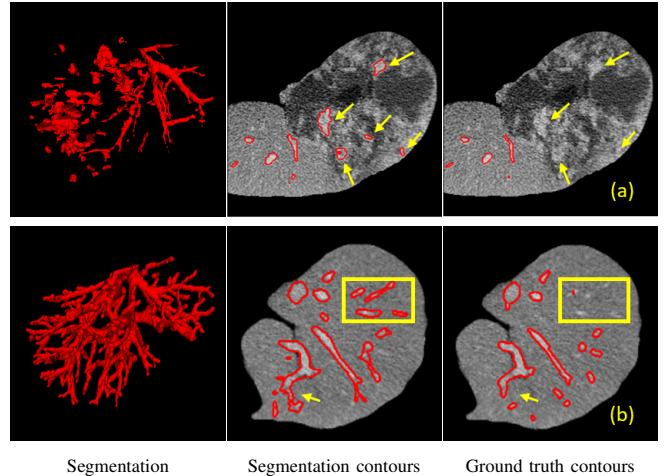


Fig. 9. **Analysis of model limitations.** (a) First row: Visualization of a failure case on the *LiVS* dataset. (b) Second row: Visualization of a failure case on the *3D-ircadb-01* dataset. In case (a) the failure is due to the contrast marked by yellow arrows around the tumors being misclassified as vessel structures. In case (b) the failure is due to the unlabeled vessels [15], [44] as highlighted in the yellow box causing lower *DSC* scores. The model also makes a mistake by predicting segmentation masks where there should not be (over-segmentation), as shown by the yellow arrow. This is caused by the inconsistency in annotations in the *3D-ircadb-01* dataset [34].

B. Accelerating diffusion inference

The number of denoising steps T in the diffusion inference is usually set to 1000 [28]. Advanced sampling methods like *DPM-Solver++* [26] can accelerate the diffusion process. In Fig. 10 we compare using the *DDPM* and *DPM-Solver++* sampling methods while testing our *GATSegDiff* model on *3D-ircadb-01* and *LiVS* datasets. In Fig. 10(a), the default *DDPM* sampling method has a higher averaged *DSC* on *3D-ircadb-01* dataset across training iterations, although *Sen* values after 140k are a bit worse than when using the *DPM-Solver++* sampling. This may be due to the ensemble scheme used for the *DPM-Solver++* sampling, which creates more segmentations. In Fig. 10(b), the *DSC* scores after 140k using *DPM-Solver++* sampling are even higher than using normal *DDPM* sampling. However, the increase in *DSC* scores comes at the cost of a decrease in *Sen* scores: the *Sen* scores of the *DPM-Solver++* are considerably lower than those of the *DDPM*. This hints to incomplete segmentations. The *DPM-Solver++* decreases the denoising steps from 1000 to 30×3 (ensemble inference 3 times), thus accelerating the inference by a factor 10 compared to *DDPM*. Yet, even when using the *DPM-Solver++*, the *DSC* scores of our *GATSegDiff* outperform the other methods in Tab. II and Tab. III.

VI. CONCLUSIONS

In this study, we focus on liver vessel segmentation from CT volumes. To this end, we propose to augment conditional diffusion models with geometric graph-structure computed at multiple resolutions. The role of the graph structure is to ensure continuity in the segmentation, across neighboring slices in the CT volume. Moreover, we use multi-scale features in the graph, thus allowing the model to focus on small vessels, that otherwise would be missed. Our proposed *GATSegDiff*

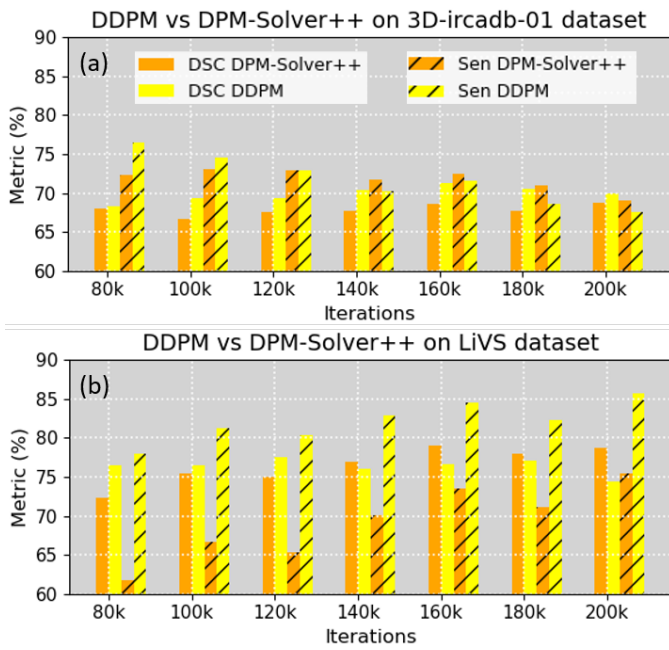


Fig. 10. **Accelerating the inference.** DSC and Sen scores across different training iterations, when using DDPM [28] and DPM-Solver++ [26] sampling scheme on the 3D-ircadb-01 and LiVS datasets. The DPM-Solver++ increases the inference speed by a factor 10 compared to DDPM, however this comes at the cost of lower DSC scores for 3D-ircadb-01 and lower Sen scores for LiVS. Overall, even when using the DPM-Solver++ solver, our method outperforms the other methods in Tab. II and Tab. III.

model achieves state-of-the-art results, improving by at least **11.67%** and **3.21%** in DSC and by at least **24.21%** and **9.11%** in Sen on two standard benchmarks: 3D-ircadb-01 [34] and LiVS [10], when compared to baselines such as MedSegDiff [41], EnsemDiff [40], Swin UNETR [12] and nnUNet [17].

REFERENCES

- [1] O.I. Alirri and A.A.A. Rahni. Survey on liver tumour resection planning system: steps, techniques, and parameters. *Journal of Digital Imaging*, 33(2):304–323, 2020. 1
- [2] F. Bieder, J. Wolleb, A. Durrer, R. Sandkühler, and P.C. Cattin. Memory-efficient 3d denoising diffusion models for medical image processing. In *Medical Imaging with Deep Learning*, 2023. 2
- [3] S. Brody, U. Alon, and E. Yahav. How attentive are graph attention networks? In *International Conference on Learning Representations*, 2022. 2, 3, 4
- [4] S. Cetin and G. Unal. A higher-order tensor vessel tractography for segmentation of vascular structures. *IEEE Transactions on Medical Imaging*, 34(10):2172–2185, 2015. 1
- [5] Y. Chen, S. Liu, and X. Wang. Learning continuous image representation with local implicit image function. In *Proceedings of the IEEE/CVF conference on computer vision and pattern recognition*, pages 8628–8638, 2021. 2, 4
- [6] Y. Cheng, X. Hu, J. Wang, Y. Wang, and S. Tamura. Accurate vessel segmentation with constrained b-snake. *IEEE Transactions on Image Processing*, 24(8):2440–2455, 2015. 1
- [7] M. Chung, J. Lee, J. W. Chung, and Y.-G. Shin. Accurate liver vessel segmentation via active contour model with dense vessel candidates. *Computer methods and programs in biomedicine*, 166:61–75, 2018. 1
- [8] Guy Disibio and Samuel W French. Metastatic patterns of cancers: results from a large autopsy study. *Archives of pathology & laboratory medicine*, 132(6):931–939, 2008. 1
- [9] O. Friman, M. Hindennach, C. Kühnel, and H.O. Peitgen. Multiple hypothesis template tracking of small 3d vessel structures. *Medical image analysis*, 14(2):160–171, 2010. 1
- [10] Z. Gao, Q. Zong, Y. Wang, Y. Yan, Y. Wang, N. Zhu, J. Zhang, Y. Wang, and L. Zhao. Laplacian salience-gated feature pyramid network for accurate liver vessel segmentation. *IEEE Transactions on Medical Imaging*, May 2023. 2, 5, 7, 8, 10
- [11] M.E. Gegúndez-Arias, A. Aquino, J.M. Bravo, and D. Marín. A function for quality evaluation of retinal vessel segmentations. *IEEE Transactions on Medical Imaging*, 31(2):231–239, 2011. 5
- [12] A. Hatamizadeh, V. Nath, Y. Tang, D. Yang, H.R. Roth, and D. Xu. Swin unetr: Swin transformers for semantic segmentation of brain tumors in mri images. In *International MICCAI Brainlesion Workshop*, pages 272–284, September 2021. 1, 2, 5, 6, 7, 10
- [13] J. Ho, A. Jain, and P. Abbeel. Denoising diffusion probabilistic models. In *Advances in neural information processing systems*, volume 33, pages 6840–6851, 2020. 1, 2, 3
- [14] H.W. Huang. Influence of blood vessel on the thermal lesion formation during radiofrequency ablation for liver tumors. *Medical physics*, 40(7):073303, 2013. 1
- [15] Q. Huang, J. Sun, H. Ding, X. Wang, and G. Wang. Robust liver vessel extraction using 3d u-net with variant dice loss function. *Computers in Biology and Medicine*, 101:153–162, 2018. 1, 2, 3, 5, 9
- [16] B. Ibragimov, D. Toesca, D. Chang, A. Koong, and L. Xing. Combining deep learning with anatomical analysis for segmentation of the portal vein for liver sbrt planning. *Physics in Medicine & Biology*, 62(23):8943, 2017. 2
- [17] F. Isensee, P. F. Jaeger, S. A. Kohl, J. Petersen, and K. H. Maier-Hein. nnu-net: A self-configuring method for deep learning-based biomedical image segmentation. *Nature methods*, 18(2):203–211, 2021. 1, 2, 3, 5, 6, 7, 10
- [18] T. Kitrungsakul, X.H. Han, Y. Iwamoto, L. Lin, A.H. Foruzan, W. Xiong, and Y.W. Chen. Vesselnet: A deep convolutional neural network with multi pathways for robust hepatic vessel segmentation. *Computerized Medical Imaging and Graphics*, 75:74–83, 2019. 1, 2
- [19] J. Lamy, O. Merveille, B. Kerautret, and N. Passat. A benchmark framework for multiregion analysis of vesselness filters. *IEEE Transactions on Medical Imaging*, 41(12):3649–3662, 2022. 1
- [20] R. Li, Y.J. Huang, H. Chen, X. Liu, Y. Yu, D. Qian, and L. Wang. 3d graph-connectivity constrained network for hepatic vessel segmentation. *IEEE Journal of Biomedical and Health Informatics*, 26(3):1251–1262, 2021. 1, 2, 4
- [21] X. Li, P. Ramadori, D. Pfister, M. Seehawer, L. Zender, and M. Heikenwalder. The immunological and metabolic landscape in primary and metastatic liver cancer. *Nature Reviews Cancer*, 21(9):541–557, 2021. 1
- [22] L. Liu, J.M. Wolterink, C. Brune, and R.N. Veldhuis. Anatomy-aided deep learning for medical image segmentation: a review. *Physics in Medicine & Biology*, 66(11):11TR01, 2021. 2
- [23] Y. Liu, J. Yu, and Y. Han. Understanding the effective receptive field in semantic image segmentation. *Multimedia Tools and Applications*, 77:22159–22171, 2018. 2
- [24] Z. Liu, Y. Lin, Y. Cao, H. Hu, Y. Wei, Z. Zhang, S. Lin, and B. Guo. Swin transformer: Hierarchical vision transformer using shifted windows. In *Proceedings of the IEEE/CVF international conference on computer vision*, pages 10012–10022, 2021. 2
- [25] J.M. Llovet, R.K. Kelley, and A. Villanueva. Hepatocellular carcinoma. *Nat Rev Dis Primers*, 7(6), 2021. 1
- [26] C. Lu, Y. Zhou, F. Bao, J. Chen, C. Li, and J. Zhu. Dpm-solver: A fast ode solver for diffusion probabilistic model sampling in around 10 steps. In S. Koyejo, S. Mohamed, A. Agarwal, D. Belgrave, K. Cho, and A. Oh, editors, *Advances in Neural Information Processing Systems*, volume 35, pages 5775–5787. Curran Associates, Inc., 2022. 6, 9, 10
- [27] D. Müller, I. Soto-Rey, and F. Kramer. Towards a guideline for evaluation metrics in medical image segmentation. *BMC Research Notes*, 15(1):210, 2022. 5
- [28] A.Q. Nichol and P. Dhariwal. Improved denoising diffusion probabilistic models. In *International Conference on Machine Learning*, pages 8162–8171. PMLR, July 2021. 1, 5, 6, 9, 10
- [29] O. Ronneberger, P. Fischer, and T. Brox. U-net: Convolutional networks for biomedical image segmentation. In *Medical Image Computing and Computer-Assisted Intervention*, pages 234–241. Springer International Publishing, 2015. 2, 3
- [30] R. Selvan, T. Kipf, M. Welling, A.G. Juarez, J.H. Pedersen, J. Petersen, and M. de Bruijne. Graph refinement based airway extraction using mean-field networks and graph neural networks. *Medical image analysis*, 64:101751, 2020. 2
- [31] S.Y. Shin, S. Lee, I.D. Yun, and K.M. Lee. Deep vessel segmentation by learning graphical connectivity. *Medical Image Analysis*, 58:101556, 2019. 2, 3

- [32] S. Shit, J.C. Paetzold, A. Sekuboyina, I. Ezhov, A. Unger, A. Zhylyka, J.P.W. Pluim, U. Bauer, and B.H. Menze. cldice-a novel topology-preserving loss function for tubular structure segmentation. In *Proceedings of the IEEE/CVF conference on computer vision and pattern recognition*, pages 16560–16569, 2021. 5, 6
- [33] R.D. Soberanis-Mukul, N. Navab, and S. Albarqouni. Uncertainty-based graph convolutional networks for organ segmentation refinement. In *Medical Imaging with Deep Learning*, pages 755–769. PMLR, 2020. 2
- [34] L. Soler, A. Hostettler, V. Agnus, A. Charnoz, J. Fasquel, J. Moreau, A. Osswald, M. Bouhadjar, and J. Marescaux. 3d image reconstruction for comparison of algorithm database: A patient specific anatomical and medical image database. 2, 5, 6, 9, 10
- [35] S. Survarachakan, E. Pelanis, Z.A. Khan, R.P. Kumar, B. Edwin, and F. Lindseth. Effects of enhancement on deep learning based hepatic vessel segmentation. *Electronics*, 10(10):1165, 2021. 1
- [36] Z. Tian, X. Li, Y. Zheng, Z. Chen, Z. Shi, L. Liu, and B. Fei. Graph-convolutional-network-based interactive prostate segmentation in mr images. *Medical physics*, 47(9):4164–4176, 2020. 2
- [37] P. Veličković, G. Cucurull, A. Casanova, A. Romero, P. Lio, and Y. Bengio. Graph Attention Networks. *International Conference on Learning Representations*, 2018. 2
- [38] X. Wang, X. Zhang, G. Wang, Y. Zhang, X. Shi, H. Dai, M. Liu, Z. Wang, and X. Meng. Transfusionnet: Semantic and spatial features fusion framework for liver tumor and vessel segmentation under jetsontx2. *IEEE Journal of Biomedical and Health Informatics*, 27(3):1173–1184, 2022. 2
- [39] J.R. Weaver. Centrosymmetric (cross-symmetric) matrices, their basic properties, eigenvalues, and eigenvectors. *The American Mathematical Monthly*, 92(10):711–717, 1985. 5
- [40] J. Wolleb, R. Sandkühler, F. Bieder, P. Valmaggia, and P.C. Cattin. Diffusion models for implicit image segmentation ensembles. In *International Conference on Medical Imaging with Deep Learning*, pages 1336–1348. PMLR, December 2022. 2, 3, 5, 6, 7, 8, 10
- [41] J. Wu, R. FU, H. Fang, Y. Zhang, Y. Yang, H. Xiong, H. Liu, and Y. Xu. Medsegdiff: Medical image segmentation with diffusion probabilistic model. In *Medical Imaging with Deep Learning*, 2023. 2, 5, 6, 7, 8, 10
- [42] M. Wu, Y. Qian, X. Liao, Q. Wang, and P.A. Heng. Hepatic vessel segmentation based on 3d swin-transformer with inductive biased multi-head self-attention. *BMC Medical Imaging*, 23(1):1–14, 2023. 1, 2
- [43] Z. Xing, L. Wan, H. Fu, G. Yang, and L. Zhu. Diff-unet: A diffusion embedded network for volumetric segmentation. *CoRR*, 2023. 2
- [44] Q. Yan, B. Wang, W. Zhang, C. Luo, W. Xu, Z. Xu, Y. Zhang, Q. Shi, L. Zhang, and Z. You. Attention-guided deep neural network with multi-scale feature fusion for liver vessel segmentation. *IEEE Journal of Biomedical and Health Informatics*, 25(7):2629–2642, 2020. 2, 5, 9
- [45] P.A. Yushkevich, J. Piven, H.C. Hazlett, R.G. Smith, S. Ho, J.C. Gee, and G. Gerig. User-guided 3d active contour segmentation of anatomical structures: Significantly improved efficiency and reliability. *Neuroimage*, 31(3):1116–1128, Jul 2006. 5
- [46] D. Zhang, S. Liu, S. Chaganti, E. Gibson, Z. Xu, S. Grbic, W. Cai, and D. Comaniciu. Graph attention network based pruning for reconstructing 3d liver vessel morphology from contrasted ct images. *CoRR*, 2020. 1, 2
- [47] R. Zhao, B. Qian, X. Zhang, Y. Li, R. Wei, Y. Liu, and Y. Pan. Rethinking dice loss for medical image segmentation. In *2020 IEEE International Conference on Data Mining (ICDM)*, pages 851–860. IEEE, 2020. 2